

# A new method to retrieve relative humidity profiles from a synergy of Raman lidar, microwave radiometer and satellite

Chengli Ji<sup>1</sup>, Qiankai Jin<sup>2</sup>, Feilong Li<sup>2</sup>, Yuyang Liu<sup>2</sup>, Zhicheng Wang<sup>1</sup>, Jiajia Mao<sup>1</sup>, Xiaoyu Ren<sup>1</sup>,  
Yan Xiang<sup>4</sup>, Wanlin Jian<sup>5,6</sup>, Zhenyi Chen<sup>\*2,3</sup> and Peitao Zhao<sup>\*1</sup>

<sup>1</sup> CMA Meteorological Observation Centre, Beijing, 100081, China

<sup>2</sup> State Environmental Protection Key Laboratory of Food Chain Pollution Control, Beijing Technology and Business University, Beijing, 100048, China

<sup>3</sup> Key Lab. of Environmental Optics & Technology, Anhui Institute of Optics and Fine Mechanics, Chinese Academy of Sciences, Hefei, 230031, China

<sup>4</sup> Institutes of Physical Science and Information Technology, Anhui University, Hefei, 230031, China

<sup>5</sup> Sichuan Meteorological Observation and Data Center, Chengdu, 610072, China

<sup>6</sup> Sichuan Meteorological Observatory Heavy rain and Drought – Floor Disaster in Plateau and Basin Key Laboratory of Sichuan Province, Chengdu, 610072, China

*\*Corresponding author:* E – mail: [zychen@btbu.edu.cn](mailto:zychen@btbu.edu.cn) (Zhenyi Chen),  
[peitaozhao@163.com](mailto:peitaozhao@163.com) (Peitao Zhao)

**Abstract** Precise continuous measurements of relative humidity (RH) vertical profiles in the troposphere have emerged as a considerable scientific issue. In recent years, a combination of diverse ground-based remote sensing devices has effectively facilitated RH vertical profiling, leading to enhancements in spatial resolution and, in certain instances, measurement accuracy. This work introduces a newly developed approach for obtaining continuous RH profiles by integrating data from a Raman lidar, a microwave radiometer, and satellite sources. RH profiles obtained using synergistic approaches are subsequently compared with radiosonde data throughout a five-month observational study in China. Our suggested method for RH profiling demonstrates optimal concordance with the best correction coefficients  $R$  of 0.94 in Huhehaote

(HHHT), 0.92 in Yibin (YB) and 0.93 in Qingyuan (QY), respectively. Accordingly, the mean bias (MB) reached the lowest values of 4.93% in HHHT, 2.63% in YB and 2.40% in QY. The mean value of RH decreased with height and presented seasonal characteristics in QY. Finally, the RH height-time evolution in a convective case was analyzed. This study firstly integrates satellite data into ground-based measurement to provide information on RH profiles in China, which may aid in further evaluating their regional characteristic and their impacts on the local ecosystem.

**Keywords:** relative humidity profiles, Raman lidar, microwave radiometer, satellite

## 1. Introduction

Relative humidity (RH) is a crucial parameter in characterizing aerosol-cloud interactions (Fan et al., 2007) and is necessary as input for weather forecasting models (Petters and Kreidenweis, 2007; Wex et al., 2008; Mochida, 2014). The combination of these RH profiles with aerosol optical data allows us to obtain hygroscopic growth factors for different aerosol types (Zieger et al., 2013; Granados et al., 2015). However, the temporal resolution of routine observations performed by weather services is rather low, typically with one or two radiosonde launches per day (Schmetz et al., 2021). And significant mesoscale weather phenomena, including the movement of frontal systems and the formation of convective boundary hygroscopic growth or clouds, transpire rapidly, making it more challenging to adequately monitor the evolution of atmospheric profiles (Kang et al., 2019; Long et al., 2023; Chen et al., 2024). Consequently, precise information with great temporal resolution is essential for examining these events.

The current Raman lidar technology enables concurrent measurements of temperature and water vapor mixing ratio profiles to derive RH profiles (Reichardt et al., 2012; Brocard et al., 2013). But it requires calibration by the use of collocated and simultaneous observations from a radiosonde or microwave radiometer (MWR) (Mattis et al., 2002; Madonna et al., 2011; Foth et al., 2015). In addition, the average error of Raman lidar is relatively small within the effective height range but limited in the higher height detection.

MWR is another way to provide atmospheric RH observations with high temporal resolution (Hogg et al., 1983; Ware et al., 2003; Zhang et al., 2024). Although MWR has a certain penetration ability for harsh weather conditions such as clouds, their vertical resolution and accuracy are not high, especially for RH which vary greatly (Xu et al., 2015). Thus it is challenging to deliver continuous high-resolution RH information with a single instrument. The synergy of complementary information from both active and passive instruments can provide a more comprehensive understanding of atmospheric processes (Stankov, 1995;

67 Furumoto et al., 2003; Delanoë and Hogan, 2008; Blumberg et al., 2015; Tuner et al., 2021).  
68 For example, when both Raman lidar and MWR are measuring collocated and simultaneously,  
69 continuous temperature, water vapor profiles and thus RH profiles can be obtained  
70 operationally (Navas-Guzmán et al., 2014; Barrera-Verdejo et al., 2016; Foth et al., 2017;  
71 Toporov et al., 2020). However, most of their algorithms primarily utilize statistical methods,  
72 performing data fusion between different instruments based on long-term time-series data from  
73 individual locations. While these approaches are suitable for observations at single stations,  
74 they lack universality when applied to scenarios requiring data integration from multiple sites  
75 or broader geographical coverage. Moreover, replacing instruments or equipment may also  
76 introduce additional inconsistencies.

77 For accurate RH profile retrieval at higher heights, satellites have global detection capabilities  
78 and are highly effective for oceanic skies and remote land areas (Zhang et al., 2022; Wang et  
79 al., 2023). For example, Wang et al. measured the subgrid-scale variability of critical relative  
80 humidity ( $RH_c$ ) to investigate the cloud parameterization based on the diagnostics from  
81 CloudSat/CALIPSO satellite data. Some deal with the retrieval of the atmospheric layer  
82 averaged relative humidity profiles using data from the Microwave Humidity Sounder (MHS)  
83 onboard the MetOp satellite (Gangwar et al., 2014). Geostationary Operational Environmental  
84 Satellite (GOES)-13 and the Moderate-Resolution Imaging Spectroradiometer (MODIS) data  
85 are also be combined to estimate hourly relative humidity at the surface level (Ramírez-  
86 Beltrán et al., 2019). Another sounder, SAPHIR, onboard MEGHA-TROPIQUES provides  
87 measurements in six water vapour channels for sounding the atmospheric humidity. Brogniez  
88 et al. (2013) and Gohil et al. (2013) have shown the potential of SAPHIR sounder in retrieving  
89 the atmospheric humidity profile.

90 But the time resolution of polar orbit satellites is determined by the repeated coverage time of  
91 the satellite orbit (Skou, et al., 2022). A single satellite can generally only achieve repeated  
92 observations twice a day, and the time resolution is also relatively low. Furthermore, few  
93 observations are available from China's satellite Fenyun (FY), to the use of synthetic retrieval  
94 of RH information. This study aims to introduce a novel technique that integrates Raman lidar,  
95 MWR, and satellite data (FY4B) using an optimum estimating methodology. It is given with a  
96 focus on two aspects: i) Evaluation of the proposed synergetic method, and ii), investigation of  
97 the RH characteristics at different heights and in different geographic regions. This paper is  
98 thus structured as follows. Descriptions of the individual equipment is presented in Section 2.  
99 Section 3 illustrates the process of the new synergetic algorithm combining the ground-based

and satellite data. Section 4 presents the RH statistic results and its time-height evolution in a strong convective case. Finally, conclusions are summarized in Section 5.

## **2. Instrumentation**

### *2.1 Raman lidar*

The Raman lidar method can assess the water vapor mixing ratio profiles through inelastic backscattering signals from nitrogen at 387 nm and from water vapor at 407 nm (Whiteman, 1992; Mattis et al., 2002; Adam et al., 2010). At the lowest height, the intersection of the laser beam with the receiver's field of view in the bistatic system is incomplete. Nevertheless, the overlap of both Raman channels is presumed to be equivalent; thus, the overlap effect could be minimal concerning water vapor measurements. The collected water vapor measurements, then along with concurrent temperature profiles from a co-located MWR allow us to obtain RH profiles. The vertical and temporal resolution of Raman lidar and other instruments are listed in Table 1.

### *2.2 Microwave Radiometer (MWR)*

The Microwave Radiometer (MWR) serves as a passive instrument designed to measure atmospheric emissions across two frequency bands within the microwave spectrum (Cimini et al., 2006; Crewell and Löhnert, 2007). There are seven channels set along the 22.235 GHz H<sub>2</sub>O absorption line. Humidity information can be extracted from these observations. The seven channels of the alternative band from 51 to 58 GHz within the O<sub>2</sub> absorption complex encompass the vertical temperature profile data. Consequently, the fully automatic MWR enables the derivation of temperature and humidity profiles with a temporal resolution of up to 5 minutes. The method for inverting temperature and humidity profiles is the neural network method in this study. It uses statistical methods to optimize the long-term average radiosonde data and relies on previous radiosonde data (Yang et al., 2023).

### *2.3 Radiosonde data*

We use radiosonde data from the China Meteorological Administration (CMA) station for reference analysis. It is located in the same place as the Raman lidar, and provides on-site measurements of atmospheric pressure, temperature, and RH. During the observing campaign, radiosondes were launched twice a day (08:00 LST and 20:00 LST). The height of the radiosonde balloon can be determined by the ascent time of the radiosonde balloon. The vertical resolution of the raw data is 3 m/layer. To match other data, the vertical resolution of the raw data is interpolated to 30 m (0-3000 m) and 250 m (3000-10000 m), respectively.

### *2.3 Satellite*

In 2016 and 2021, China successfully deployed two second-generation geostationary meteorological satellites, Fengyun-4A (FY4A) and Fengyun-4B (FY4B), both equipped with the Geostationary Interferometric Infrared Sounder (GIIRS). The GIIRS therefore became the first geostationary orbiting meteorological satellite (Yang et al., 2023). This approach could achieve the detection of weather systems across China and its neighboring regions with high temporal and spatial resolution. So it enables a more comprehensive understanding of the atmospheric vertical structure, including the retrieval of atmospheric temperature profiles for 1000 m layers and moisture profiles for 2000 m layers (Yang et al., 2017), respectively. In comparison to FY4A, the GIIRS on FY4B exhibits a broader spectral range, improved spectral resolution in the long-wave IR band, and superior radiometric calibration accuracy and detection sensitivity (Sufeng et al., 2022). Specifically, the temporal resolution of GIIRS has enhanced from 2.5 hours for FY4A to 2 hours for FY4B, and the spatial resolution has progressed from 16000 m to 12000 m at nadir. The atmospheric humidity profiles utilized in this study, derived from GIIRS, are generated through the neural network algorithm created by the National Satellite Meteorological Centre (NSMC) (Bai et al., 2022). The data is available online: <http://fy4.nsmc.org.cn/nsmc/en/theme/FY4B.html> (accessed on 12 December 2024).

### 3. Methods and evaluation

#### 3.1 Lidar, MWR and satellite synergetic algorithm

This study aims to obtain a continuous time series of RH profiles by integrating ground-based remote sensing techniques, including Raman lidar, MWR, and satellite data, in a straightforward manner to facilitate a wide range of applications. The retrieval process involves a systematic four-step algorithm that integrates the Raman lidar water mixing ratio profile and MWR brightness temperatures along with satellite data. The retrieval framework is shown as in Fig. 1 and the retrieval process is detailed in the following paragraphs.

Step 1: Data quality control. Data with quality control codes of 0 and 1 for FY4B and 0 for ground-based remote sensing data is selected. The lidar only retains data with a SNR value greater than 3. The threshold value of the SNR is set as 3 based on our extensive comparisons with radiosonde data from CMA's long-term observations. The results indicate that selecting lidar signals with signal-to-noise ratios (SNR) >3 can significantly improve the consistency between retrieved RH profiles and radiosonde measurements. So in the data selection period, the Raman signal starts with the first SNR greater than 3 and ends with five consecutive SNRs less than 3. The real-time observing data are designated as  $R_{\text{radio}}$ ,  $R_{\text{lidar}}$ ,  $R_{\text{MWR}}$  and  $R_{\text{satellite}}$  in Fig. 2.

Step 2: Data spatial-temporal matching. This process aims to match the above quality-controlled data with the radiosonde data at a height of 0-10000 m in time and space before the synergetic algorithm. For the time matching, temperature from MWR and water vapor data from Raman lidar are selected corresponding to the radiosonde data time (00:80 LST and 20:00 LST). In terms of spatial matching, the FY4B data is selected from the nearest grid point to the ground observing station for the horizontal scale. The data at vertical heights are interpolated to the resolution of 30 m (0-3000 m) and 250 m (3000-10000 m).

Step 3: Correction coefficient determination. The deviation between the temperature and humidity data of satellites and ground-based remote sensing data at each height is quantitatively calculated and analyzed to prepare for the optimal stitching process in the next step. Here the deviation of lidar, MWR and FY4B is designated as  $D_{\text{lidar}}$ ,  $D_{\text{MWR}}$  and  $D_{\text{satellite}}$ , respectively.

$$D_{\text{lidar}} = R_{\text{lidar}} - R_{\text{radio}} \quad (1)$$

$$D_{\text{MWR}} = R_{\text{MWR}} - R_{\text{radio}} \quad (2)$$

$$D_{\text{satellite}} = R_{\text{satellite}} - R_{\text{radio}} \quad (3)$$

The correction coefficients  $C_{\text{lidar}}$ ,  $C_{\text{MWR}}$  and  $C_{\text{satellite}}$  are calculated as follows

$$C_{\text{Lidar}} = (|D_{\text{satellite}}| + |D_{\text{MWR}}|) / [2 * (|D_{\text{satellite}}| + |D_{\text{MWR}}| + |D_{\text{lidar}}|)] \quad (4)$$

$$C_{\text{MWR}} = (|D_{\text{satellite}}| + |D_{\text{lidar}}|) / [2 * (|D_{\text{satellite}}| + |D_{\text{MWR}}| + |D_{\text{lidar}}|)] \quad (5)$$

$$C_{\text{satellite}} = (D_{\text{MWR}} + D_{\text{lidar}}) / [2 * -(|D_{\text{satellite}}| + |D_{\text{MWR}}| + |D_{\text{lidar}}|)] \quad (6)$$

Step 4: Synergetic algorithm iteration and evaluation: Based on the above spatial-temporal data matching and correction coefficients calculation at different heights, a dynamic optimal stitching algorithm (Fig. 2) is conducted. To ensure the independence between the tested sample and the true value, the temperature and humidity profiles of the current time are fused using the correction coefficient of the previous time, and then compared with the radiosonde data at the same time for evaluation. The correlation coefficient (R), the root mean square error (RMSE), and mean bias (MB) are used as inspection indexes. Finally, the retrieved RH information  $S_{\text{RH}}$  could be obtained through the following formula.

$$S_{\text{RH}} = R_{\text{satellite}} * C_{\text{satellite}} + R_{\text{MWR}} * C_{\text{MWR}} + R_{\text{lidar}} * C_{\text{Lidar}} \quad (7)$$

From the process we can see that compared to these existing techniques, our new method not only incorporates satellite data but also dynamically determines optimal fusion coefficients. Because the fusion coefficients are dynamically determined by comparing the deviations from

other measurements with the reference of radiosonde, it highlights that this new algorithm is real-time calibrated. And it can guarantee the device model independence and geographical adaptability. Thus it eliminates constraints imposed by equipment specifications or observation locations, ensuring broad applicability across diverse scenarios.

### 3.2 Error analysis

To evaluate the performance of the synergetic algorithm for RH profiles, a comparative analysis was conducted between retrieved values and actual radiosonde measurements. Let  $N$  represent the total number of samples. The measured value is designated as  $O_i$ , with  $i$  representing the sample label. The value obtained through the new synergetic algorithm is designated as  $G_i$ . The evaluation indicators consist of MB, mean absolute bias (MAB) and RMSE are defined by the following formulas:

$$MB = \frac{\sum_{i=1}^N (G_i - O_i)}{N} \quad (8)$$

$$MAB = \frac{\sum_{i=1}^N |G_i - O_i|}{N} \quad (9)$$

$$RMSE = \sqrt{\frac{\sum_{i=1}^N (G_i - O_i)^2}{N}} \quad (10)$$

## 4. Results

### 4.1 General statistic information

A five-month data set has been chosen for a statistical analysis of RH profiles. The observation period spans from July 1 to November 30, 2024. The observing elements are RH data from 47 stations in China (yellow circles in Fig. 3) at the height of 0-10000 m. To investigate RH retrieval accuracy, we provide the comparison results of four methods (lidar, MWR, satellite, and synergetic algorithm) utilizing the radiosonde data as the reference at 47 sites in Table 2. Then Huhehaote (HHHT, northern China), Yibin (YB, middle China) and Qingyuan (QY, southern China) are selected as 3 representative sites (red stars in Fig. 3) for more detailed analysis, as shown in Fig. 4 and Table 3.

Generally, the synergetic algorithm at 47 sites presents the maximum correlation coefficient  $R$  value of 0.98 with the minimum RMSE of 5.27% in Table 2. For three representative sites, the regression line from the synergetic algorithm at all heights similarly provides the best fitting results, with the largest correlation coefficients  $R$  of 0.94, 0.92 and 0.93 in HHHT, YB and QY respectively (Table 3). The correlation coefficient  $R$  for lidar measurement follows with

marginally higher values of 0.83 in HHHT, 0.86 in YB and 0.86 in QY, indicating its greater applicability compared to other single instruments. MWR presents the lowest R of 0.74 and 0.80 in HHHT and YB, while performing better ( $R = 0.75$ ) than that from satellite ( $R = 0.66$ ) in QY. In terms of RMSE, the lidar-, MWR- and satellite-derived RH all show values larger than 18% at three sites. The synergistic use of a multi-source algorithm decreases the RMSE down to the lowest value of 10% in HHHT.

The regression line for lidar and MWR in HHHT, as illustrated in Fig. 4, exhibits a slope that is less than that of the one-to-one line. This implies that greater variations arise with increased RH in HHHT. Though the synergetic algorithm also presents similar trends, its RMSE decreased to 26% in HHHT. The regression line of MWR and lidar in YB and QY are larger than the one-to-one line, indicating the larger bias for less humid.

As RH vertical profiles are height-dependent, Fig. 5 presents the MB profiles observed at different heights in terms of four methods. Generally, the MB in the RH of lidar in the lower troposphere (below 3000 m) outperforms the other two single methods (MWR and satellite) at three sites. No significant biases between radiosonde and lidar are noticeable. Specifically, the lowest MB values (4.93% in HHHT, 2.63% in YB and 2.40% in QY) in the comprehensive region of the tropospheric region are achieved when lidar data is incorporated into the synergetic algorithm. This is because lidar is an active remote sensing technology with more accuracy compared to MWR and satellite. The lidar data's efficacy is enhanced at heights below 3000 m when integrated with data from other sources within the boundary layer.

However, the MB from lidar increased drastically above this height, up to the highest value 28.67% in HHHT, 29.91% in YB and 20.09 % in QY. It is reasonable that the atmosphere changes so fast that radiosonde do not assess exactly the same air mass as lidar. In the meantime, lidar is increasingly constrained at elevated heights because of a decreased SNR. Hence lidar is more trustworthy in the lower layer, i.e. below 3000 m.

In contrast, the MB from satellite (FY4B) over 3000 m varied steadily within the range of approximately 15% at three sites. Therefore the satellite data in the far height range would be more reliable and could be employed in the synergetic algorithm at higher layers. Compared to lidar and satellite, the MB from MWR gives the largest uncertainty in HHHT at all heights. This may result from the discrepancy between the temperature recorded by the radiosonde and that obtained from the MWR in HHHT. However, it yields relatively less variation than lidar and satellite in YB and QY. Anyway, the synergetic method gives the best result for over three observing sites at almost all heights. And accurate measurements of RH vertical profiles provided here are highly beneficial for analyzing the hygroscopic growth of local aerosols.



261 The sources of the discrepancy can stem from several aspects. First, although all instruments  
262 are co-located in the ground, radiosondes deviate at higher heights, and signals can be  
263 disrupted if clouds are present. Second, satellites provide gridded data, requiring the selection  
264 of ground observation points closest to its grid's latitude and longitude, which introduces  
265 uncertainty. Finally, both MWR and satellite are passive remote sensing technologies, which  
266 are inherently less precise than active remote sensing. Besides the inherent hardware difference,  
267 the errors during the retrieval process (e.g., neural networks for MWR) are also unavoidable.

#### 268 *4.2 Mean monthly analysis*

269 RH mean monthly vertical profiles have been derived from the synergistic method illustrated  
270 in Fig. 6. Because RH profiles were retrieved from water ratio profiles and temperature profiles.  
271 For this property, the RH seasonal behavior may be more complicated. For example, no  
272 obvious seasonal behavior of RH profiles is found in HHHT or YB. However, QY still  
273 presents the most likely seasonal characteristic at most of the heights, with the highest mean  
274 values in summer at 1000-2000 m (80.65% in July) and lowest values at 7000-10000 m in late  
275 autumn (20.50% in November) in Fig. 6e-f. The elevated RH observed in QY's summer may  
276 be related to the sufficient water vapor and large transport volume as QY is located in coastal  
277 areas. So the characteristic of QY would be more dependent on water vapor.

278 For comparison, HHHT and YB are relatively random. Over 3000 m in HHHT (Fig. 6a-b), RH  
279 in August shows predominantly high values with the highest value of 65.37% at 5000-7000 m.  
280 Different from HHHT and QY, the RH profiles in November of YB interestingly show the  
281 highest values (83.95%) in the lower atmosphere (0-1000 m) in Fig. 6c-d. It suggests the  
282 reduced temperatures observed in autumn of YB promote proximity to saturation conditions,  
283 resulting in elevated RH values in November. It is also worth noting that RH above 3000 m in  
284 November of YB decreases dramatically as height increases, with the minimum RH of 13.91%  
285 at 7000-10000 m. That could be explained by more rapid fluctuations in the water vapor  
286 density and temperature in YB in the higher layer under the control of the subtropical monsoon  
287 climate zone. Anyway, this plot illustrates a clear decrease in the RH values with heights at  
288 three sites.

289 Though there is no obvious RH uncertainty caused by regional differences, we found that QY  
290 exhibits the predominant seasonal feature throughout most heights. In contrast, no discernible  
291 seasonal characteristics in RH profiles are observed in HHHT or YB. Thus we believe diverse  
292 atmospheric circulation patterns and geographical environments could result in regional  
293 variations in RH values.

#### 294 *4.3 Case analysis*

295 We selected two different severe convective events in YB (one hailfall and one heavy  
296 precipitation) for comparison in Fig. 7. At 23:00 LST on April 15, a thunderstorm with strong  
297 winds and hail occurred. The synergetic algorithm retrieved RH profile showed that before  
298 22:00 LST, the RH was high (around 90%) at 3000 m height, low (20%-50%) between 3500 m  
299 and 8000 m, and above 80% between 8000 m and 9000 m (Fig. 7a). This indicates that before  
300 the severe convection, the upper and lower layers were relatively moist, while the middle layer  
301 (3500 m-8000 m) was relatively dry (red arrow in Fig. 7a). Such a condition favors the  
302 evaporation and cooling of ice particles descending from the upper atmosphere, leading to  
303 refreezing and hail formation.

304 In contrast, the RH profile from 25 May to 26 May showed that the entire troposphere  
305 (0-10000 m) presented high RH values (>70%) starting at 19:00 LST, which was conducive to  
306 heavy precipitation (Fig. 7b). According to ground station observations, YB recorded an hourly  
307 rainfall of 52 mm at 21:00 LST, along with gale-force winds of 23 m/s (9th grade). Most areas  
308 in YB experienced precipitation, with localized heavy rainstorms. From the above two cases,  
309 we can see that the RH in the middle troposphere can be used to distinguish between hail and  
310 heavy precipitation during severe convective events.

## 311 **5. Conclusion**

312 This study presents relative humidity (RH) measurements with a developed synergetic  
313 algorithm with the combination of Raman lidar, MWR, and satellite at three sites (northern  
314 China, middle of China and southern China) from 1 July to 31 November. The methodology  
315 for obtaining RH from the synergetic algorithm was introduced. The five-month field  
316 campaign was performed and linear regression between the lidar, MWR, satellite, synergetic  
317 algorithm and radiosonde data at the range 0-10000 m was presented to testify the accuracy.

318 Strong correlations of RH values over 0.9 were observed between radiosonde measurements  
319 and profiles derived from the synergetic approach at three representative sites in China. The  
320 lowest MB values (4.93% in HHHT, 2.63% in YB and 2.40% in QY) are observed when lidar  
321 data is integrated into the synergetic algorithm, which highlights the accuracy of the lidar data  
322 below 3000 m. However, the MB from lidar increased drastically above this height, which  
323 suggests the greater applicability of satellite or MWR in the middle and higher layers. In terms  
324 of the seasonal characteristic, QY exhibits the predominant seasonal feature throughout most  
325 heights, with peak mean values of 80.65% in July at 1000-2000 m and minimal values of  
326 20.50% in November at 7000-10000 m.

327 These results validate the capabilities of the newly developed method to deliver accurate  
328 measurements of RH information throughout the troposphere. It also explores the potential of  
329 satellite data integration for RH profile retrieval for the first time. However, there are still  
330 problems with individual data at certain times during the fusing process. For example, there are  
331 few effective data filtered by quality control methods for FY4B data. Therefore, the matching  
332 accuracy and more high-quality FY4B data will be improved in future development.

### 333 **Declaration of Competing Interest**

334 The authors declare that they have no known competing financial interests or personal  
335 relationships that could have appeared to influence the work reported in this paper.

### 336 **Data availability**

337 Raman lidar, MWR, satellite, radiosonde and other auxiliary data used to generate the results  
338 of this paper are available from the authors upon request (email: zychen@btbu.edu.cn).

### 339 **Acknowledgments**

340 This work was supported by the Innovation and Development Special Project of China  
341 Meteorological Administration (No. CXFZ2024J011 and CXFZ2024J057), National Key  
342 Research and Development Program of China (No. 2024YFC3711701) and the project  
343 (Simulation of cloud lidar echo signal and study on cloud microphysics characteristics) from  
344 Aerospace Information Innovation Research Institute, Chinese Academy of Sciences. The  
345 authors thank the colleagues who participated in the operation of the lidar system at our site.  
346 We also acknowledge the CMA for the satellite (FY4B) data, radiosonde data  
347 (<https://ladsweb.modaps.eosdis.nasa.gov>), and the European Center for Medium - Range  
348 Weather Forecasts (ECMWF) for the ERA5 reanalysis data (<https://climate.copernicus.eu>  
349 /climate - reanalysis).

350

### 351 **References**

- 352 Adam, M., Demoz, B.B., Whiteman, D. N., Venable, D.D., Joseph, E., Gambacorta, A., Wei, J.,  
353 Shephard, M.W., Milosevich, L. M., Barnet, C. D., Herman, R. L., Fitzgibbon, J., and  
354 Connell, R.: Water Vapor Measurements by Howard University Raman lidar during the  
355 WAVES 2006 Campaign, J. Atmos. Ocean. Tech., 27, 42-60,  
356 <https://doi.org/10.1175/2009JTECHA1331.1>, 2010.
- 357 Bai, W., Zhang, P., Liu, H., Zhang, W., Qi, C., Ma, G., and Li, G.: A fast piecewise-defined  
358 neural network method to retrieve temperature and humidity profile for the vertical  
359 atmospheric sounding system of FengYun-3E satellite. IEEE Trans. Geosci. Remote Sens.  
360 2023, 61, 4100910.

361 Barrera-Verdejo, M., Crewell, S., Löhnert, U., Orlandi, E., and Di Girolamo, P.: Ground-based  
362 lidar and microwave radiometry synergy for high vertical resolution absolute humidity  
363 profiling, *Atmos. Meas. Tech.*, 9, 4013-4028, <https://doi.org/10.5194/amt-9-4013-2016>,  
364 2016.

365 Blumberg, W.G., Turner, D.D., Löhnert, U., and Castleberry, S.: Ground based temperature and  
366 humidity profiling using spectral infrared and microwave observations, Part II: Actual  
367 retrieval performance in clear-sky and cloudy conditions, *J. Appl. Meteorol.*, 54,  
368 2305-2319, 2015.

369 Brocard, E., Jeannet, P., Begert, M., Levrat, G. Philipona, R., Romanens, G. and Scherrer, S.C.:  
370 Upper air temperature trends above Switzerland 1959-2011, *J. Geophys. Res. Atmos.*, 118,  
371 4303-4317, doi:10.1002/jgrd.50438, 2013.

372 Brogniez H., Kirstetter P. E., and Eymard L., Expected improvements in the atmospheric  
373 humidity profile retrieval using the Megha-Tropiques microwave payload, *Quarterly*  
374 *Journal of the Royal Meteorological Society.* 139(673), 842-851,  
375 doi.org/10.1002/qj.1869, 2-s2.0-84879241188, 2013.

376 Chen, Z.Y., Ji, C. L., Mao, J. J., Wang, Z. C., Jiao, Z. M., Gao, L. N., Xiang, Y. and Zhang, T.  
377 S.: Downdraft influences on the differences of PM<sub>2.5</sub> concentration: insights from a mega  
378 haze evolution in the winter of northern China, *Environ. Res. Lett.*, 19, 014042, 2024.

379 Cimini, D., Hewison, T., Martin, L., Güldner, J., Gaffard, C., and Marzano, F.: Temperature  
380 and humidity profile retrievals from ground-based microwave radiometers during  
381 TUC., *Meteor. Z.*, 15, 45-56, <https://doi.org/10.1127/0941-2948/2006/0099>, 2006.

382 Crewell and U. Lohnert: Accuracy of boundary layer temperature profiles retrieved with  
383 multifrequency multiangle microwave radiometry, *IEEE T. Geosci. Remote*, 45,7,  
384 2195-2201, doi: 10.1109/TGRS.2006.888434, 2007.

385 Delanoë, J., and Hogan R. J.: A variational scheme for retrieving ice cloud properties from  
386 combined radar, lidar, and infrared radiometer., *J. Geophys. Res.*, 113 (D7): D07204, doi:  
387 10.1029/2007JD009000, 2008.

388 Fan, J. Zhang, R., Li, G., Tao, W.K., and Li, X.: Effects of aerosols and relative humidity on  
389 cumulus clouds, *J. Geophys. Res.*, 112, D14204, <https://doi.org/10.1029/2006JD008136>,  
390 2007.

391 Foth, A., Baars, H., Di Girolamo, P., and Pospichal, B.: Water vapor profiles from Raman lidar  
392 automatically calibrated by microwave radiometer data during HOPE, *Atmos. Chem.*  
393 *Phys.*, 15, 7753-7763, <https://doi.org/10.5194/acp-15-7753-2015>, 2015.

394 Foth, A. and Pospichal, B.: Optimal estimation of water vapour profiles using a combination of  
395 Raman lidar and microwave radiometer, *Atmos. Meas. Tech.*, 10, 3325-3344,  
396 <https://doi.org/10.5194/amt-10-3325-2017>, 2017.

397 Furumoto, J., Kurimoto, K. and Tsuda, T.: Continuous observations of humidity profiles with  
398 the Mu Radar-RASS combined with GPS and radiosonde measurements., *J. Atmos.*  
399 *Oceanic. Technol.*, 20, 23-41, 2003.

400 Gangwar, R. K., Gohil, B. S., Mathur, A. K., Retrieval of Layer Averaged Relative Humidity  
401 Profiles from MHS Observations over Tropical Region, *J. Atmos. Sci.*, 645970  
402 (10), [doi.org/10.1155/2014/645970](https://doi.org/10.1155/2014/645970), 2014.

403 Gohil B. S., Gairola R. M., Mathur A. K., Varma A. K., Mahesh C., Gangwar R. K., and Pal P.  
404 K., Algorithms for retrieving geophysical parameters from the MADRAS and SAPHIR  
405 sensors of the Megha-Tropiques satellite: Indian scenario, *Q. J. Roy. Meteor. Soc.* 139  
406 (673), 954-963, [doi.org/10.1002/qj.2041](https://doi.org/10.1002/qj.2041), 2-s2.0-84879226042, 2013.

407 Granados-Muñoz, M. J., Navas-Guzmán, F., Bravo-Aranda, J. A., Guerrero-Rascado, J.L.,  
408 Lyamani, H., Valenzuela, A., Titos, G., Fernández-Gálvez, J., and Alados-Arboledas, L.:  
409 Hygroscopic growth of atmospheric aerosol particles based on active remote sensing and  
410 radiosounding measurements: selected cases in southeastern Spain, *Atmos. Meas. Tech.*, 8,  
411 705-718, <https://doi.org/10.5194/amt-8-705-2015>, 2015.

412 Hogg, D., Decker, M., Guiraud, F., Earnshaw, K., Merritt, D., Moran, K., Sweezy, W., Strauch,  
413 R., Westwater, E., and Little, G.: An automatic profiler of the temperature, wind and  
414 humidity in the troposphere, *J. Appl. Meteorol.*, 22, 807-831, 1983.

415 Long, L., He, L., Li, J. B., Zhang, W. L. and Zhang, Y.X.: Climatic characteristics of  
416 mesoscale convective systems in the warm season in North China. *Meteorol. Atmos.*  
417 *Phys.*, 135, 21, <https://doi.org/10.1007/s00703-023-00958-1>, 2023.

418 Kang, Y.Z., Peng, X.D., Wang, S.G., Hu, Y.L., Shang, K.Z., and Lu, S.: Observational analyses  
419 of topographic effects on convective systems in an extreme rainfall event in Northern  
420 China, *Atmos., Res.*, 229, 127-144, 2019.

421 Madonna, F., Amodeo, A., Boselli, A., Cornacchia, C., Cuomo, V., D'Amico, G., Giunta, A.,  
422 Mona, L., and Pappalardo, G.: CIAO: the CNR-IMAA advanced observatory for  
423 atmospheric research, *Atmos. Meas. Tech.*, 4, 1191-1208, [doi:10.5194/amt-4-1191-2011](https://doi.org/10.5194/amt-4-1191-2011),  
424 2011.

425 Mattis, I., Ansmann, A., Althausen, D., Jaenisch, V., Wandinger, U., Müller, D., Arshinov, Y.F.,  
426 Bobrovnikov, S.M., and Serikov, I.B.: Relative-humidity profiling in the troposphere with  
427 a Raman lidar., *Appl. Opt.*, 41, 6451-6462, [doi:10.1364/AO.41.006451](https://doi.org/10.1364/AO.41.006451), 2002.

428 Mochida, M.: Simultaneous measurements of hygroscopic property and cloud condensation  
 429 nucleus activity of aerosol particles of marine biogenic origin, Western Pacific Air-Sea  
 430 Interaction Study, 71-81, America, American Geophysical Union,  
 431 <https://doi.org/10.5047/w-pass.a01.008>, 2014.

432 Navas-Guzmán, F., Fernández-Gálvez, J. Granados-Muñoz, M.J., Guerrero-Rascado, J. L.,  
 433 Bravo-Aranda, J. A., and Alados-Arboledas, L.: Tropospheric water vapour and relative  
 434 humidity profiles from lidar and microwave radiometry, *Atmos. Meas. Tech.*, 7,  
 435 1201-1211, 2014.

436 Petters, M.D. and Kreidenweis, S.M.: A single parameter representation of hygroscopic growth  
 437 and cloud condensation nucleus activity, *Atmos. Chem. Phys.*, 7, 1961-1971,  
 438 <https://doi.org/10.5194/acp-7-1961-2007>, 2007.

439 Ramírez- Beltrán, N. D., Salazar, C. M., Castro Sánchez, J. M., and González, J. E.: A satellite  
 440 algorithm for estimating relative humidity, based on GOES and MODIS satellite data. *Int.*  
 441 *J. Remote Sens.*, 40(24), 9237–9259. <https://doi.org/10.1080/01431161.2019.1629715>,  
 442 2019.

443 Reichardt, J., Wandinger, U., Klein, V., Mattis, I., Hilber, B., and Begbie, R.: RAMSES:  
 444 German meteorological service autonomous Raman lidar for water vapor, temperature,  
 445 aerosol, and cloud measurements, *Appl. Opt.* 51, 8111-8131,  
 446 <https://doi.org/10.1364/AO.51.008111>, 2012.

447 Schmetz, J.: Good things need time: Progress with the first hyperspectral sounder in  
 448 geostationary orbit, *Geophys. Res. Lett.*, 48, e2021GL096207, 2021.

449 Stankov, B.B., Martner, B.E., and Politovich, M.K.: Moisture profiling of the cloudy winter  
 450 atmosphere using combined remote sensors, *J. Atmos. Ocean. Technol.*, 12 , 488-510,  
 451 1995.

452 Skou, N., Søbjærg, S.S. and Kristensen, S.S.: Future high-performance spaceborne microwave  
 453 radiometer systems, *IEEE Geoscience and Remote Sensing Letters*, 19, 1-5, doi:  
 454 10.1109/LGRS.2021.3118082, 2022.

455 Wang, S.F., Lu, F., and Feng, Y.T.: An Investigation of the Fengyun-4A/B GIIRS performance  
 456 on temperature and humidity retrievals., *Atmos.* ,13, 1830, 2022.

457 Toporov, M., and U. Löhnert: Synergy of satellite- and ground-based observations for  
 458 continuous monitoring of atmospheric stability, liquid water path, and integrated water  
 459 vapor: theoretical evaluations using reanalysis and neural networks, *J. Appl. Meteor.*  
 460 *Climatol.*, 59, 1153-1170, <https://doi.org/10.1175/JAMC-D-19-0169.1>, 2020

461 Turner, D.D. and Löhnert, U.: Ground-based temperature and humidity profiling: combining  
 462 active and passive remote sensors, *Atmos. Meas. Tech.*, 14, 3033-3048,  
 463 <https://doi.org/10.5194/amt-14-3033-2021>, 2021.

464 Wex, H., Stratmann, F., Hennig, T., Hartmann, S., Niedermeier, D., Nilsson, E., Ocskay, R.,  
 465 Rose, D., Salma, I., and Ziese, M.: Connecting hygroscopic growth at high humidities to  
 466 cloud activation for different particle types, *Environ. Res. Lett.*, 3, 035004, 1-10, 2008.

467 Ware, R., Carpenter, R., Guldner, J., Liljegren, J., Nehrkorn, T., Solheim, F., and  
 468 Vandenberghe, F.A.: Multi-channel radiometric profiles of temperature, humidity and  
 469 cloud liquid, *radio Sci.*, 38, 8079-8032, 2003.

470 Wang, X., Miao, H., Liu, Y., Bao, Q., He, B., Li, J., and Zhao, Y.: The use of satellite  
 471 data-based ‘critical relative humidity’ in cloud parameterization and its role in modulating  
 472 cloud feedback. *J. Adv. Model. Earth Sy.*, 14,  
 473 e2022MS003213. <https://doi.org/10.1029/2022MS003213>, 2022.

474 Wang, Z.Z., Wang, W.Y., Tong, X.L., Zhang, Z., Liu, J.Y., Lu, H.H., Ding, J., Wu, Y.T.:  
 475 Progress in spaceborne passive microwave remote sensing technology and its application  
 476 (in Chinese), *Chin. J. Space. Sci.*, 43(6): 986-1015, doi: 10.11728/cjss2023.06.yg15,  
 477 2023.

478 Whiteman, D.N., Melfi, S.H., and Ferrare, R.A.: Raman lidar system for the measurement of  
 479 water vapor and aerosols in the earth’s atmosphere, *Appl. Optics*, 31, 3068-3082,  
 480 <https://doi.org/10.1364/AO.31.003068>, 1992.

481 Xu, G. R., B. K., Zhang, W.G., Cui, C.G., Dong, X.Q., Liu, Y.Y. and Yan, G.P.: Comparison  
 482 of atmospheric profiles between microwave radiometer retrievals and radiosonde  
 483 soundings., *J. Geophys. Res. Atmos.*, 120, 10, 313-10,323,  
 484 <https://doi.org/10.1002/2015JD023438>, 2015.

485 Yang, J., Zhang, Z., Wei, C., Lu, F., and Guo, Q.: Introducing the new generation of Chinese  
 486 geostationary weather satellites, Fengyun-4. *Bull., Am. Meteorol. Soc.* 98, 1637-1658,  
 487 2017.

488 Yang, W., Chen, Y., Bai, W., Sun, X., Zheng, H., and Qin, L.: Evaluation of temperature and  
 489 humidity profiles retrieved from Fengyun-4B and implications for typhoon assimilation  
 490 and forecasting, *Remote Sens.* 15, 5339. <https://doi.org/10.3390/rs15225339>, 2023.

491 Yang, J. B., Chen, K., Xu, G. R., Gui, L. Q., Lang, L., Zhang, M.Y., Jin, F., Zhang, R. M., and  
 492 Sun, C.Y.: Research on neural network training retrieval based on microwave radiometer  
 493 observed brightness temperature data set, *Torrential Rain Disaster (in Chinese)*, 41,  
 494 477-487, <https://doi.org/10.3969/j.issn.1004-9045.2022.04.012>, 2022.

495 Zhang, L., Liu, M., He, W., Xia, X.G., Yu, H.N., Li, S., X., and Li, J.: Ground passive  
496 microwave remote sensing of atmospheric profiles using WRF simulations and machine  
497 learning techniques., J. Meteorol. Res. 38, 680-692  
498 <https://doi.org/10.1007/s13351-024-4004-2>, 2024.

499 Zhang, Z., Dong, X. and Zhu, D.: Optimal channel selection of spaceborne microwave  
500 radiometer for surface pressure retrieval over Oceans., J. Atmos. Oceanic Technol., 39,  
501 1857-1868, <https://doi.org/10.1175/JTECH-D-21-0121.1>, 2022.

502 Zieger, P., Fierz-Schmidhauser, R., Weingartner, E., and Baltensperger, U.: Effects of relative  
503 humidity on aerosol light scattering: results from different European sites, Atmos. Chem.  
504 Phys., 13, 10609-10631, <https://doi.org/10.5194/acp-13-10609-2013>, 2013.

505

506 **List of Tables**

507 **Table 1** Instruments and monitoring parameters

508

509 **Table 2** Assessment of the accuracy of four RH retrieval results (lidar, MWR, satellite and  
510 synergetic algorithm) compared with radiosonde at 47 sites in China.

Comparison with radiosonde	Number of sample	R	MB (%)	MAB (%)	RMSE (%)
lidar	192111	0.91	0.56	6.7	10.67
MWR	192111	0.82	-1.49	10.79	14.31
satellite	192111	0.74	1.08	13.19	17.02
syngenetic algorithm	192111	0.98	0.42	3.24	5.27

511

512 **Table 3** The same as Table 2 but at three representative sites in China.

HHHT (northern China)	Comparison with radiosonde	Number of sample	R	RMSE (%)
	lidar	3771	0.83	20
	MWR	3771	0.74	25
	satellite	3771	0.76	24
	syngenetic algorithm	3771	0.94	10
YB (middle China)	lidar	7542	0.86	19
	MWR	7542	0.80	26
	satellite	7542	0.83	29
	synergetic algorithm	7542	0.92	12



QY (southern China)	lidar	8110	0.86	18
	MWR	8110	0.75	19
	satellite	8110	0.66	21
	synergetic algorithm	8110	0.93	11

## List of figures

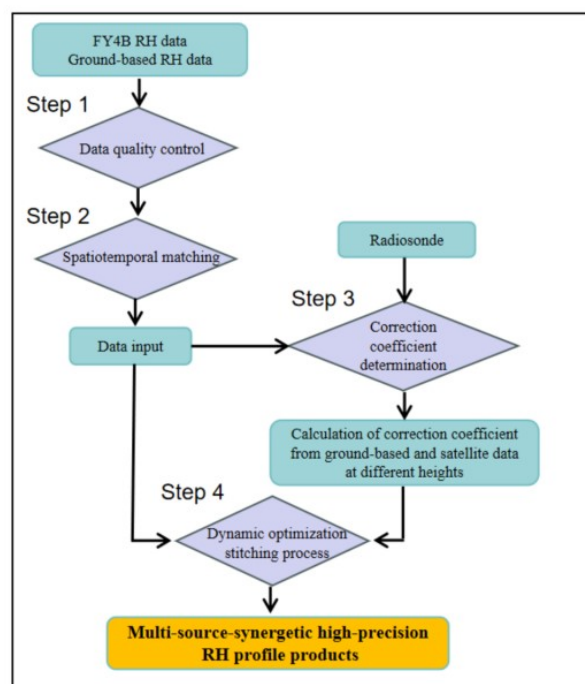


**Fig. 1** Sketch of the retrieval scheme. Details are given in the text.

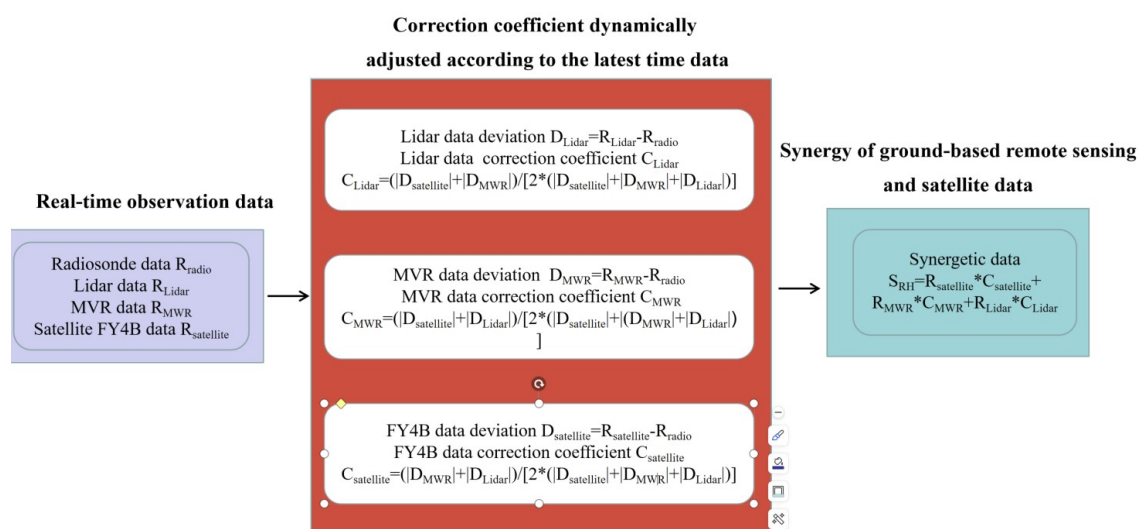


**Fig. 2** The dynamic optimal stitching process

525

526

527

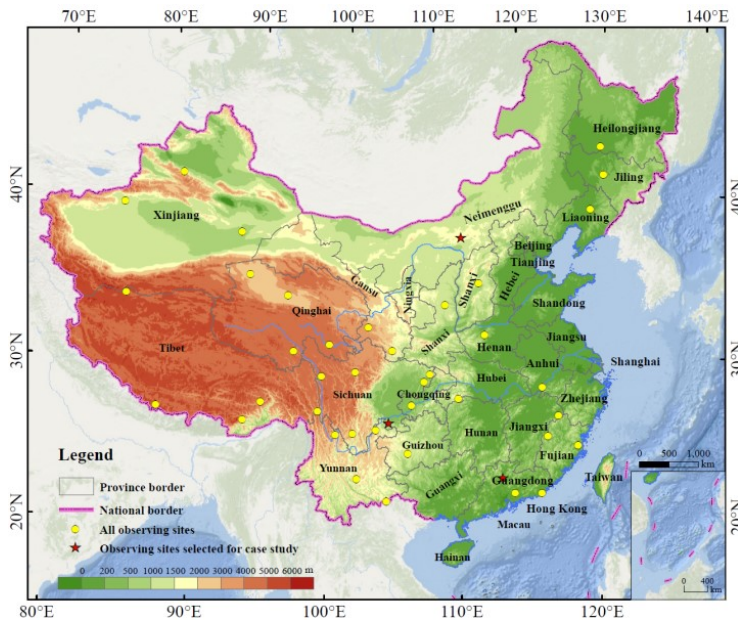
528

529

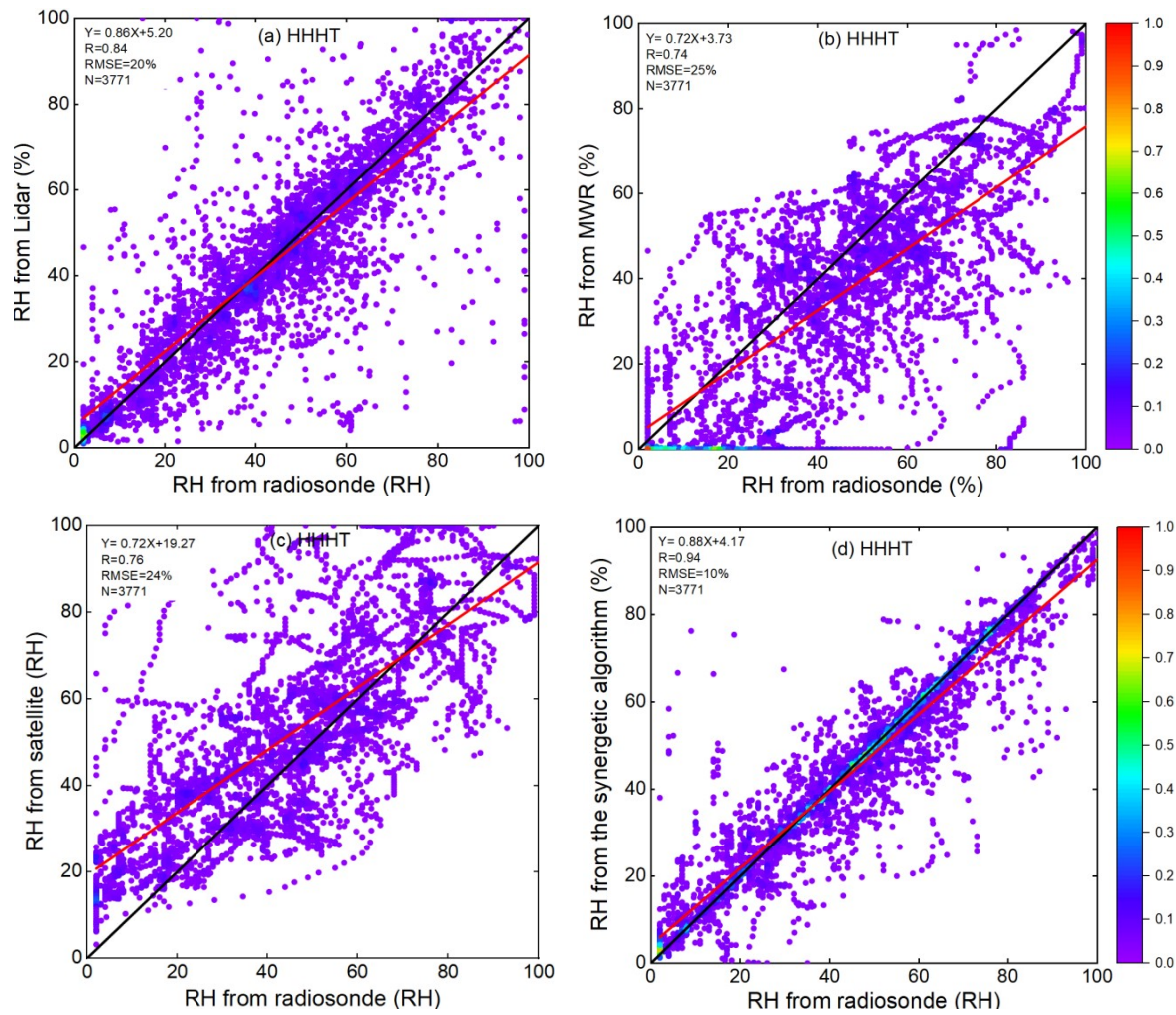
530

531

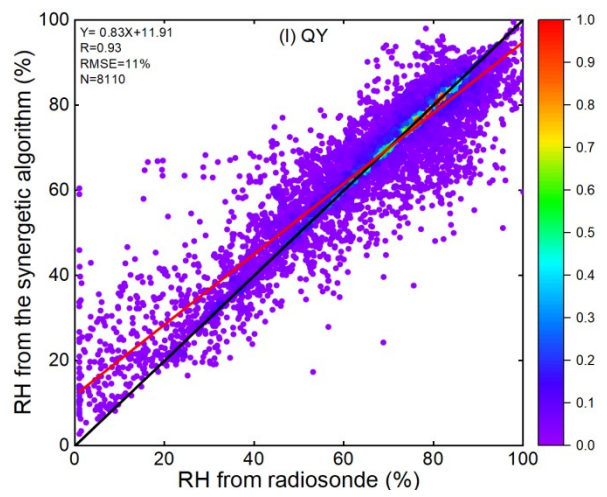
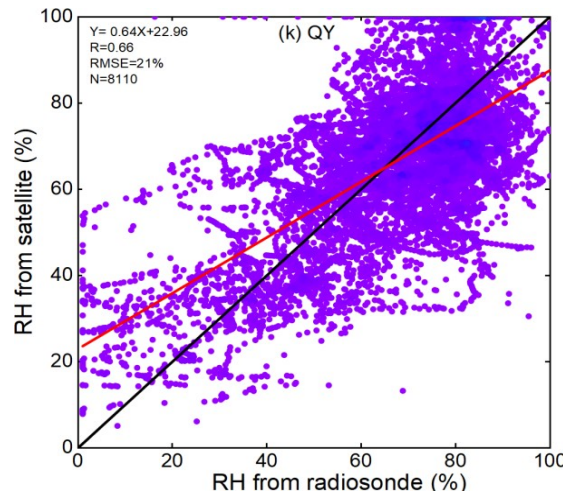
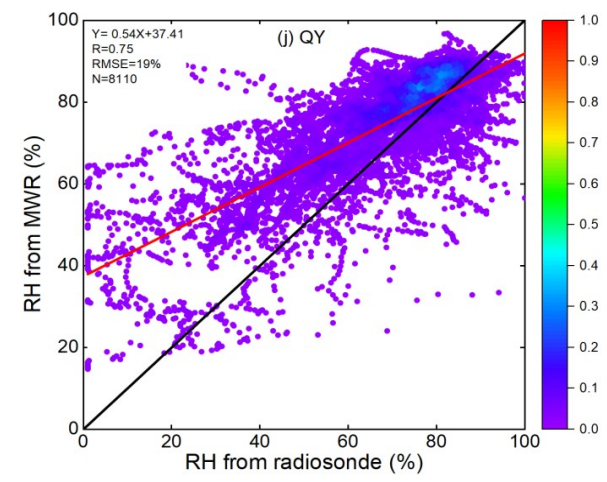
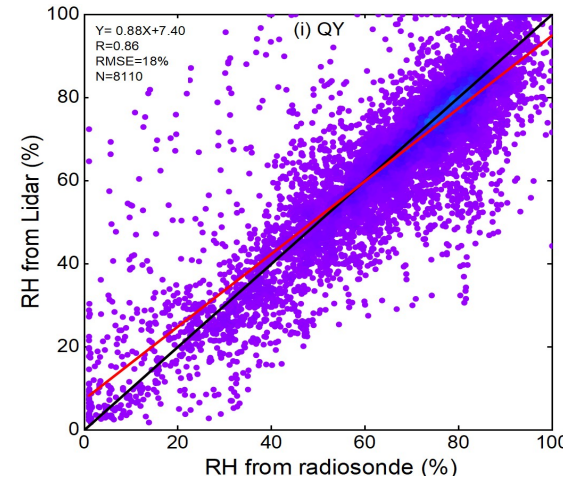
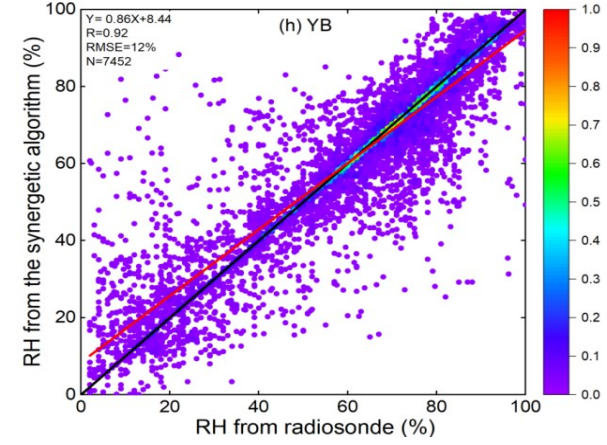
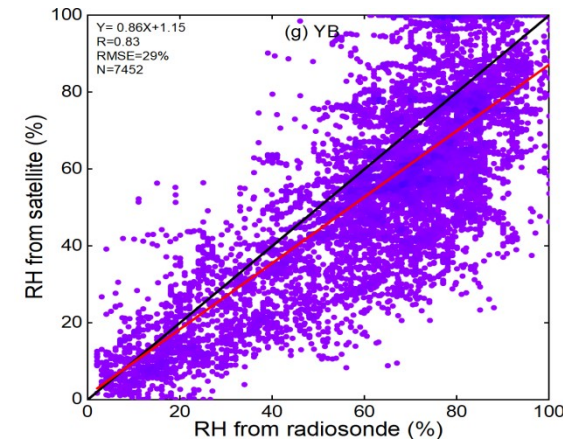
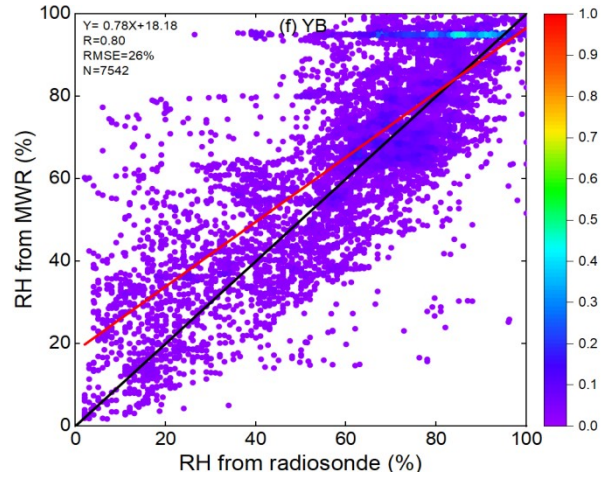
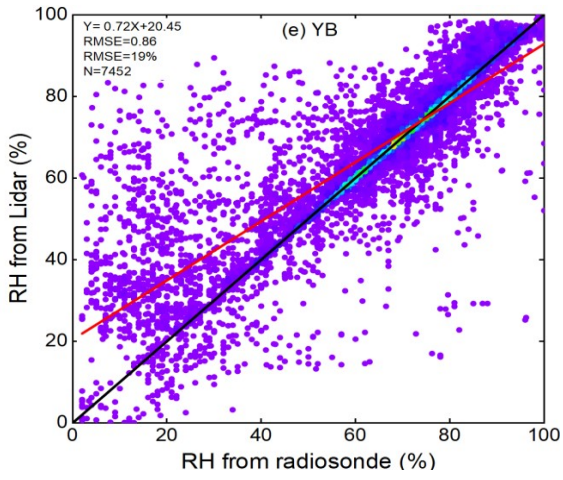
532



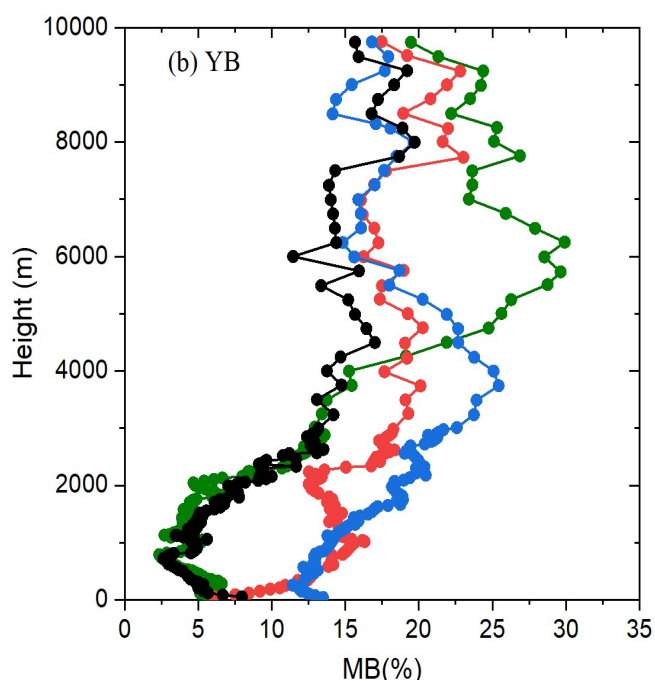
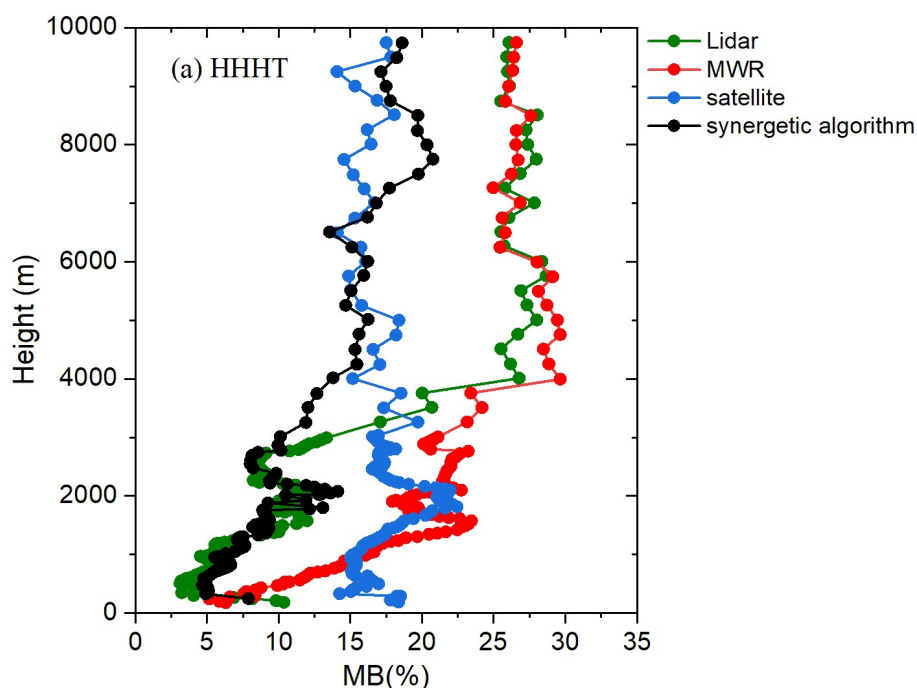
**Fig. 3** The observing sites (yellow circles) and three selected sites (red stars) for statistics and case studies are marked in the

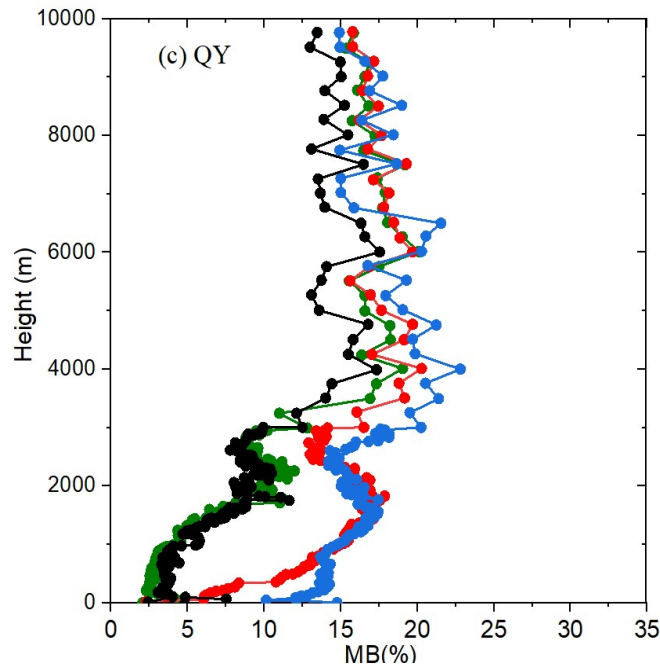




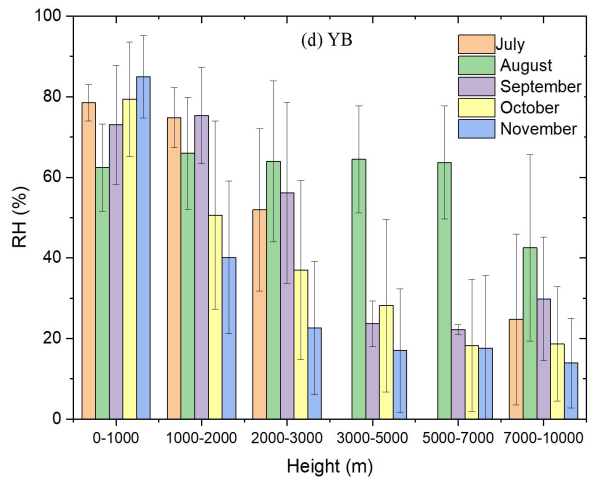
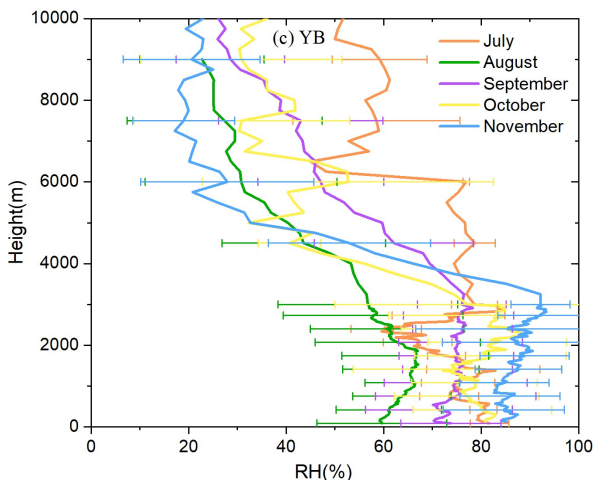
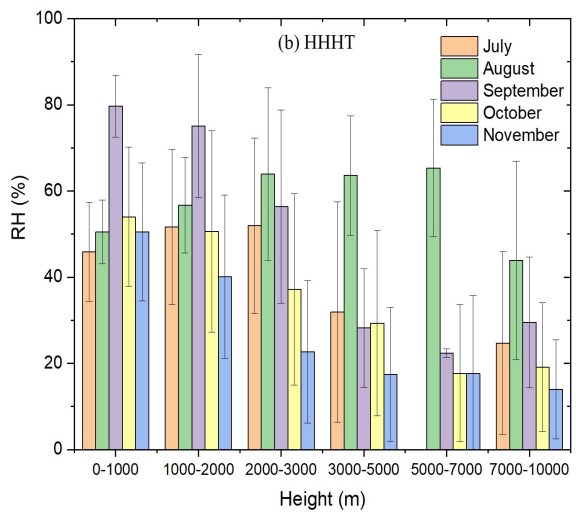
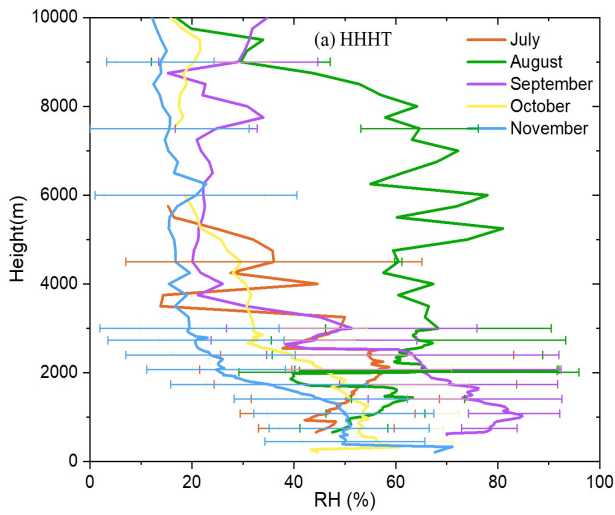


537 **Fig. 4** Four-methods-retrieved RH results (lidar, MWR, satellite and synergetic algorithm)  
 538 compared with radiosonde at three sites in China from 1 July to 31 November 2024. (a)  
 539 Comparison between lidar and radiosonde in HHHT, (b) Comparison between MWR and  
 540 radiosonde in HHHT, (c) Comparison between satellite and radiosonde HHHT, (d)  
 541 Comparison between synergetic algorithm and radiosonde in HHHT; (e)-(h), the same as (a)-(d)  
 542 but in YB. (i)-(l), the same as (a)-(d) but in QY. The red line shows the regression line. The  
 543 black line is the one-to-one line.

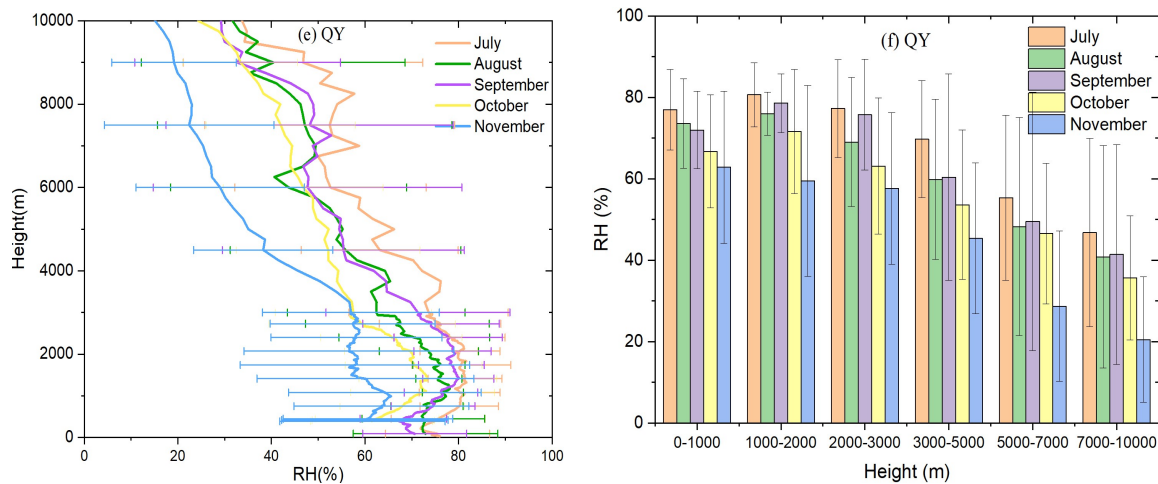




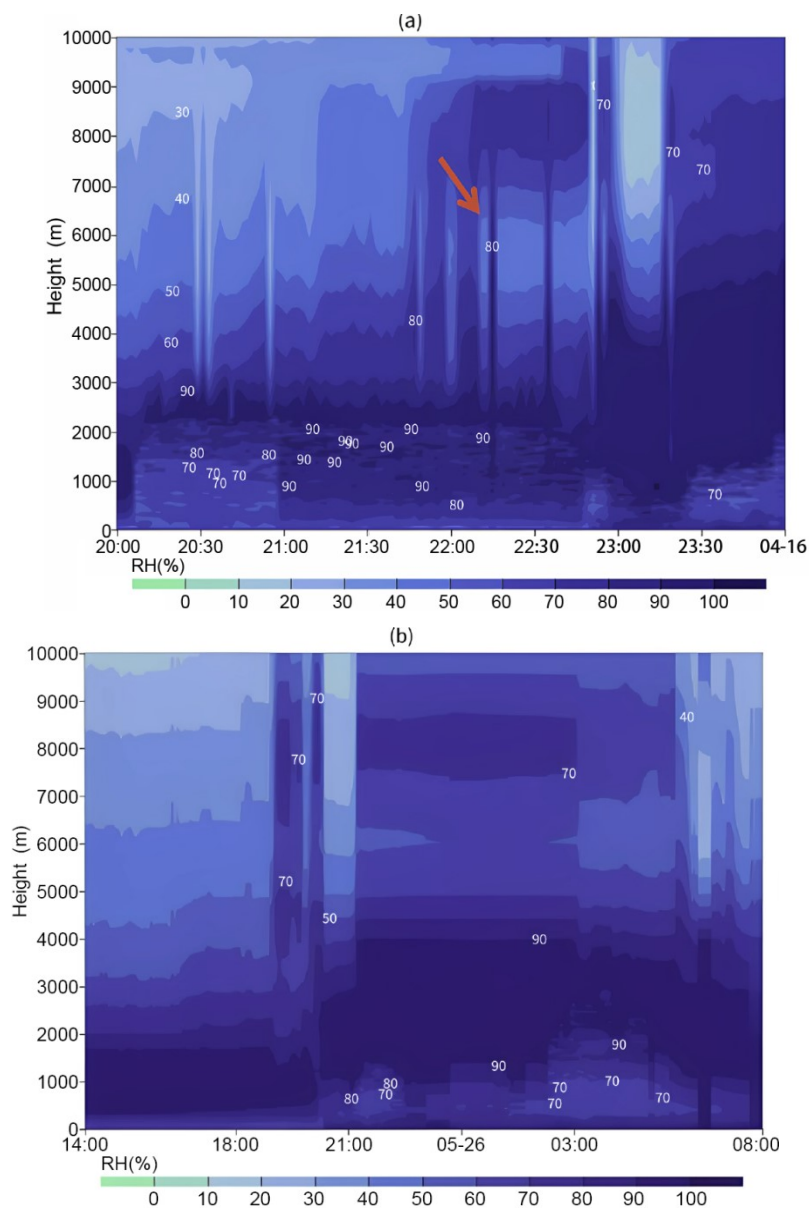
**Fig. 5** RH vertical mean bias (MB) profiles retrieved from lidar, MWR, satellite and synergetic algorithm compared to the radiosonde data in (a) HHHT, (b) YB and (c) QY.







**Fig. 6** RH Monthly vertical profiles (left) and monthly mean values for different heights (right) in (a)-(b) HHHT, (c)-(d)YB and (e)-(f) QY. The error bars indicate the standard deviation.



559 **Fig. 7** Height-time display of RH from the synergetic retrieval during two convective cases (a)  
560 from 20:00 LST to 23:30 LST 15 April and (b) from 14:00 LST 25 May to 08:00 LST 26 May  
561 2024 in YB. The red arrow indicates the less humidity in the layer when the hailfall occurred in  
562 the first convective case.